CORE
Metadata, citation and similar papers at core.ac.uk
Provided by Nottingham ePrints

Fiber orientation-dependent white matter contrast in gradient echo MRI

Samuel Wharton and Richard Bowtell[1]

Sir Peter Mansfield Magnetic Resonance Centre, School of Physics and Astronomy, University of Nottingham, Nottingham NG7 2RD, United Kingdom

Edited by Adriaan Bax, National Institutes of Health, Bethesda, MD, and approved September 25, 2012 (received for review June 29, 2012)

Recent studies have shown that there is a direct link between the orientation of the nerve fibers in white matter (WM) and the contrast observed in magnitude and phase images acquired using gradient echo MRI. Understanding the origin of this link is of great interest because it could offer access to a new diagnostic tool for investigating tissue microstructure. Since it has been suggested that myelin is the dominant source of this contrast, creating an accurate model for characterizing the effect of the myelin sheath on the evolution of the NMR signal is an essential step toward fully understanding WM contrast. In this study, we show by comparison of the results of simulations and experiments carried out on human subjects at 7T, that the magnitude and phase of signals acquired from WM in vivo can be accurately characterized by (*i*) modeling the myelin sheath as a hollow cylinder composed of material having an anisotropic magnetic susceptibility that is described by a tensor with a radially oriented principal axis, and (*ii*) adopting a two-pool model in which the water in the sheath has a reduced T_2 relaxation time and spin density relative to its surroundings, and also undergoes exchange. The accuracy and intrinsic simplicity of the hollow cylinder model provides a versatile framework for future exploitation of the effect of WM microstructure on gradient echo contrast in clinical MRI.

Gradient echo (GE) MRI is widely used in imaging the human brain, because both the phase and magnitude of the complex NMR signal measured with GE sequences can be used to create high-resolution images that show strong contrast between different types of brain tissue (1). Recent studies have shown that there is a direct link between the orientation of the nerve fibers in white matter (WM) with respect to the magnetic field and the contrast observed in magnitude and phase images (2-6). Although the origin of this link is currently not fully understood, orientation-dependent contrast is of great interest because it could offer researchers access to a new diagnostic tool for investigating tissue microstructure using MRI.

It has recently been suggested that the myelin sheaths that surround axons are the dominant source of WM contrast in GE MRI (7, 8). Creating an accurate model for characterizing the effect of the myelin sheath on the evolution of the magnitude and phase of the NMR signal is consequently an essential step toward fully understanding WM contrast and its relationship to fiber orientation. Such a model must incorporate two main features: (*i*) a representation of the microscopic spatial variation of resonant frequency, due to the myelin compartment—isotropic and anisotropic magnetic susceptibility effects (2, 9, 10) and chemical exchange of protons between water and macromolecules (11, 12), have been proposed as mechanisms through which myelin could perturb the resonant frequency in WM; (*ii*) a signal-weighting scheme to account for the reduced T_2 relaxation time constant of the myelin water relative to that of water found outside the myelin sheath (13–15).

In this study, we show by comparison of the results of simulations and experiments that the fiber orientation dependence of the magnitude and phase of signals acquired from WM in vivo can be accurately characterized by (*i*) modeling the myelin sheath as a hollow cylinder composed of material having an anisotropic susceptibility that is described by a tensor with a radially oriented principal axis, and (*ii*) adopting a two-pool model in which the water in the sheath has a reduced T_2 relaxation constant and effective spin density relative to its surroundings, and also undergoes exchange.

Results

Frequency Difference Mapping. The excellent contrast seen in phase images means that phase mapping is a potentially useful tool for investigating the structure of WM (1, 2, 9). However, phase contrast is nonlocal, in the sense that sources of field perturbation located outside a given voxel affect the phase measured inside that voxel, making it difficult to draw clear inferences about the relationship between phase variation and the underlying tissue microstructure (16). Here, we therefore first focus on frequency difference mapping, which is a technique for creating phase-based contrast that is insensitive to nonlocal effects (*SI Text*). Frequency difference mapping involves generating phase maps from GE data acquired at multiple echo times, converting these to frequency maps via scaling by echo time (TE), and then calculating the difference from a reference frequency map. In a voxel that contains multiple water compartments that experience different frequency offsets and have different T_2 values, the phase of the average signal does not necessarily scale linearly with TE. As a consequence, the apparent frequency of the voxel is TE dependent, yielding a nonzero contribution in the frequency difference map (FDM). In contrast, frequency offsets generated by nonlocal field sources are similar in all compartments in a voxel and so produce an average phase that varies linearly with TE. Nonlocal effects are consequently eliminated in the FDM. Because the signal from myelin water decays with a time constant of less than 20 ms (13, 15), an FDM that shows the difference in frequency measured at short and long TE in the 0- to 30-ms range will be sensitive to WM microstructure.

This sensitivity is illustrated in Fig. 1, which shows high-resolution frequency maps acquired from the human brain at 7T using TE values of 5 ms (Fig. 1*A*) and 25 ms (Fig. 1*B*). It is evident from these maps and the associated FDM (Fig. 1*C*) that there are significant TE-dependent changes in the apparent frequency in WM regions, which result in generally negative values of the frequency difference, Δf. Averaging Δf over the imaging volume in three healthy male subjects (20–30 y in age) gave values of 0.03 ± 0.05 and -1.22 ± 0.04 Hz in grey matter (GM) and WM, respectively. Comparison with Fig. 1*D*, which shows a fiber orientation map created using diffusion tensor imaging (DTI), indicates that particularly negative Δf values occur in the large fiber bundles oriented perpendicular to B_0, such as the corpus callosum and optic radiations. These preliminary results therefore suggest that the

Author contributions: S.W. and R.B. designed research, performed research, analyzed data, and wrote the paper.

The authors declare no conflict of interest.

This article is a PNAS Direct Submission.

Freely available online through the PNAS open access option.

[1]To whom correspondence should be addressed. E-mail: richard.bowtell@nottingham.ac.uk.

This article contains supporting information online at www.pnas.org/lookup/suppl/doi:10.1073/pnas.1211075109/-/DCSupplemental.

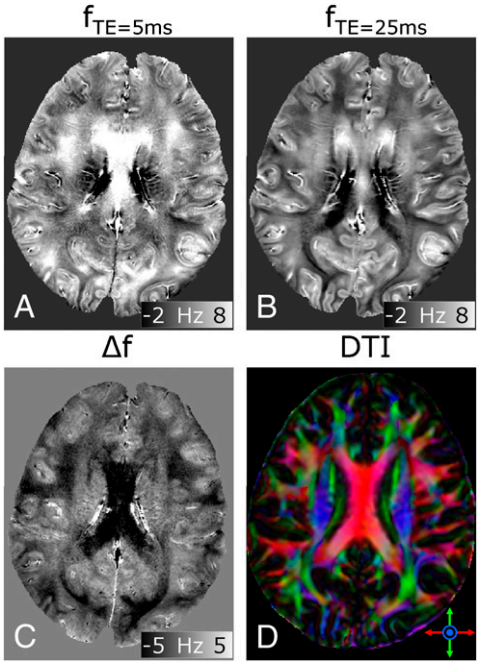

Fig. 1. Axial image data illustrating the steps followed in generating a FDM. A frequency map is created from short TE (5 ms) phase data, $f_{TE\,=\,5\ ms}$ (*A*). Another frequency map is formed from long TE (25 ms) phase data, $f_{TE\,=\,25\ ms}$ (*B*). These maps were produced by scaling high-pass-filtered phase images by TE and then setting the average frequency in cerebrospinal fluid to zero. An FDM is then created by subtracting the short TE frequency map from the long TE frequency map, $\Delta f = f_{TE\,=\,25\ ms} - f_{TE\,=\,5\ ms}$ (*C*). DTI fiber orientation map that has been converted into red/green/blue values and weighted by the FA maps (*D*). The fiber orientation is color-coded such that red is left/right, green is anterior/posterior, and blue is foot/head. Particularly large frequency differences occur in the corpus callosum where the nerve fibers are perpendicular to B_0 (central red region in *D*).

TE-dependent frequency differences, though negligible in GM, are significant, generally negative, and fiber orientation dependent in WM.

Orientation-Dependent WM Contrast. To investigate further the effect of fiber orientation on the temporal evolution of magnitude and frequency difference data, five healthy male subjects aged 20–30 were imaged using a 3D multiecho, GE acquisition at 7 T, yielding 32 image datasets with TE values ranging from 2 to 33 ms. FDM were created by subtracting a reference map, formed by averaging the frequency maps associated with the first four TE values, from each phase-based frequency map. Fig. 2 shows the variation of the normalized WM magnitude signal (Fig. 2*A*), and of Δf (Fig. 2*B*), with TE. Data are divided into five groups based on the fiber orientation, defined by the angle, θ, between the local fiber direction (extracted from DTI data) and the static field, B_0. The signal magnitude decays more rapidly as the fiber orientation changes from parallel to perpendicular to B_0, as has been previously described (3–5), whereas Δf decreases monotonically from approximately zero at TE = 3 ms to generally negative values for TE = 33 ms at a rate that is strongly dependent on the local fiber orientation. The frequency difference values at long TE range from slightly positive, $\Delta f = 0.01 \pm 0.22$ Hz, for fibers parallel to B_0, to strongly negative, $\Delta f = -1.66 \pm 0.14$ Hz, for perpendicular fibers.

Hollow Cylinder Fiber Model. The fiber model adopted here (Fig. 3*A*) represents the myelin sheath as an infinite hollow cylinder, with an inner radius, r_i, and outer radius, r_o, oriented at an angle, θ, to B_0. Two water pools were considered (Fig. 3*B*): (*i*) a small pool corresponding to the myelin water in the cylindrical annulus, whose signal is characterized by a transverse relaxation time constant, $T_{2\text{-SP}}$, and a reduced relative spin density, ρ; (*ii*) a large pool representing the water both inside and outside the myelin sheath, with a relative spin density of 1 and transverse relaxation time constant, $T_{2\text{-LP}}$.

The signal evolution was modeled by simulating the spatially varying frequency perturbation due to the myelin sheath, taking account of three different contrast mechanisms: (*i*) isotropic magnetic susceptibility; (*ii*) chemical exchange; and (*iii*) anisotropic magnetic susceptibility. Expressions for the frequency variation were formed for the different mechanisms (*SI Text*). Because the model uses an infinite cylinder approximation, the frequency perturbations are axially invariant and can be fully represented by their variation in a plane perpendicular to the axis of the hollow cylinder. Chemical exchange of protons between water and exchange sites on macromolecules, such as those found at the surface of myelin bilayers (17), can result in a small shift, $\Delta\omega_E$, of the water resonant frequency (12). The effect of this exchange is included in the model by introducing a parameter, $E = \Delta\omega_E/\gamma B_0$, representing the fractional exchange-induced frequency shift in the myelin sheath relative to the surrounding spaces. Calculation of the spatially varying frequency perturbation due to a hollow cylinder of isotropic susceptibility is straightforward (10), but the frequency perturbation due to anisotropic susceptibility is more complex to evaluate.

The highly ordered lipid molecules within the myelin sheath form the most likely source of anisotropic magnetic susceptibility (18), since similar lipid structures have been shown to exhibit anisotropic magnetic properties (19, 20). The lipids are packed together in bilayers, which spiral around the axon to form the myelin sheath. The long, aliphatic lipid chains are consequently radially aligned, leading to the expectation that the susceptibility tensor at each location is cylindrically symmetrical with a radially oriented principal axis (18). In the reference frame in which its principal axis is aligned with the *x*-direction, the susceptibility tensor, $\underline{\chi}$, can be written as shown in Fig. 3*C*, where χ_I and χ_A define the magnitudes of the isotropic and anisotropic susceptibility. The calculation of the frequency perturbation due to this form of anisotropy in the susceptibility is detailed in *SI Text*. The calculation involves forming the gradient of the magnetic scalar potential, followed by the addition of an (isotropic) sphere of Lorentz correction (21). Expressions describing the frequency perturbation due to the different mechanisms are listed in Table 1.

Fig. 4 shows maps of the frequency perturbations produced by the hollow cylinder, with its principal axis parallel ($\theta = 0°$) and

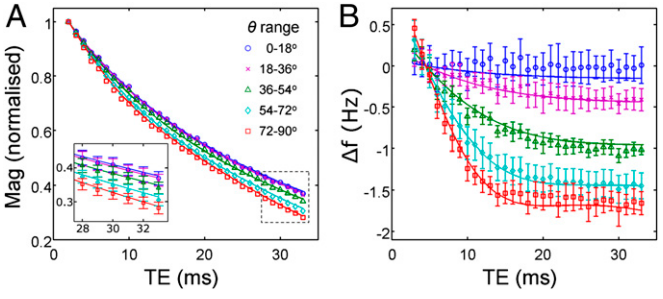

Fig. 2. Plots of the average normalized WM magnitude signal against TE, for different fiber orientations relative to B_0, characterized by an angular θ range (*A*). An expanded segment of the plot is shown with error bars (*Inset*). The corresponding averaged frequency difference is also shown for each θ range (*B*). The simulated signal evolution plots for the hollow cylinder model that achieved the lowest residual fit to the data ($\chi_I + E + \chi_A$ in Table 2) are shown as solid lines in *A* and *B*.

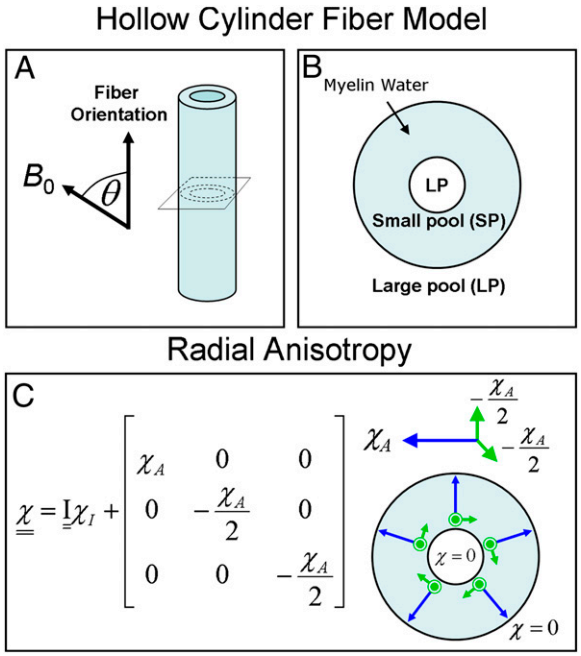

Fig. 3. Schematic of the hollow cylinder model. Nerve fibers are modeled as infinite hollow cylinders oriented at angle, θ, to B_0 (*A*). A two-pool model is adopted where the cylindrical annulus forms the small pool of myelin water, and the large pool corresponds to the external and internal spaces (*B*). The susceptibility of the myelin sheath is anisotropic and described by a cylindrically symmetric tensor in which the principal axis is radially oriented (*C*).

perpendicular ($\theta = 90°$) to B_0, as a result of the three different mechanisms: isotropic susceptibility (χ_I), exchange (E), and radial anisotropic susceptibility (χ_A). Simulations were carried out for a g-ratio (14), r_i/r_o, of 0.8. Inspection of the maps and Table 1 makes evident a few key points: exchange generates a frequency offset that is independent of orientation and position (i.e., homogeneous) and confined to the material of the hollow cylinder (Fig. 4 *B* and *E*). When the hollow cylinder is parallel to B_0, anisotropic and isotropic susceptibility generate homogeneous frequency offsets within the material, whose sizes depend on the magnitude of the effective susceptibility along the cylinder's axis (Fig. 4 *A* and *C*). When the hollow cylinder is perpendicular to B_0, isotropic susceptibility generates no frequency offset inside the hollow cylinder, but produces a spatially varying (inhomogeneous) frequency offset outside the cylinder and a similar sort of variation in the material of the cylinder, superimposed upon a uniform (homogeneous) frequency offset (Fig. 4*D*). The frequency variation generated by the radial anisotropic susceptibility for the perpendicular case is rather different, with a nonzero, homogeneous frequency offset inside the hollow cylinder and an average offset of the opposite sign produced in the material of the cylinder, along with a weak inhomogeneous field, also present outside the cylinder (Fig. 4*F*). When the cylinder is oriented at intermediate angles to B_0, the frequency perturbation is a simple weighted superposition of the parallel and perpendicular maps.

Fitting the Hollow Cylinder Model to Frequency Difference Data. Simulations were carried out to characterize the effect of microstructure on the GE signal evolution in WM. The signal was calculated for four different combinations of the mechanisms by which myelin could perturb the frequency in the hollow cylinder model, and fitted to the magnitude and frequency difference data shown in Fig. 2. These combinations were (*i*) χ_I, (*ii*) $\chi_I + E$, (*iii*) $\chi_I + \chi_A$, and (*iv*) $\chi_I + E + \chi_A$. The frequency perturbations due to the different mechanisms (Fig. 4) were linearly superposed for simulations involving more than one source of contrast, and the signal was formed by summing weighted contributions from a 2D grid in the standard manner (22), including points within a circular region outside the myelin annulus whose radius was dictated by the fiber volume fraction (FVF). The phase of the signal at each time point was converted into a frequency value using the same method as was applied to the experimental data. In addition to χ_I, E, and χ_A, other variable parameters in the simulations were (*i*) the g-ratio; (*ii*) the T_2 values of the two water pools, $T_{2\text{-LP}}$ and $T_{2\text{-SP}}$; and (*iii*) the relative proton density, ρ, in the myelin sheath. To simplify the fitting procedure, the FVF was fixed as 0.5, based on literature values (14).

An iterative fitting procedure was then carried out for each of the four combinations. In each iteration, separate field maps were produced for each of the five θ-ranges used to group the in vivo data shown in Fig. 2. A reduced chi-squared residual was then formed by comparing the evolution of the simulated and measured magnitude and frequency-difference data. The parameter values that yielded the lowest residual for each combination are shown in Table 2. Simulations based on isotropic susceptibility effects only (χ_I) failed to yield a successful fit to the measured data and are therefore not described in the table. The best fit (solid lines in Fig. 2) was achieved by including the effect of exchange, isotropic susceptibility, and radial anisotropic susceptibility ($\chi_I + E + \chi_A$). The plots in Fig. 2 indicate that the orientation-dependent evolution of the magnitude and frequency difference can be well characterized by the hollow cylinder model. However, because several mechanism combinations can produce a good fit to the experimental data (Table 2), further information is needed to identify which of the proposed effects underlies the experimentally measured contrast.

Calculating the Nonlocal Field. The nonlocal field perturbation, resulting from the anatomical distribution of gray and white matter, potentially provides such information, because it is dependent on the magnetic susceptibility of the myelin sheath and in particular upon the type of susceptibility anisotropy that is present (18). By subtracting the TE-dependent local frequency offset, calculated using the hollow cylinder model (solid lines in Fig. 2), on a voxel-by-voxel basis from the frequency maps measured at different TE values, and then averaging the differences, a single frequency map that represents the effects of

Table 1. Expressions describing the frequency perturbation in the hollow cylinder model

Mechanism/region	$r < r_i$	$r_i < r < r_o$	$r > r_o$
$\chi_I \times$	0	$\frac{1}{2}\left(c^2 - \frac{1}{3} - s^2\cos 2\phi\left(\frac{r_i^2}{r^2}\right)\right)$	$\frac{s^2\cos 2\phi}{2}\left(\frac{r_o^2 - r_i^2}{r^2}\right)$
$E \times$	0	1	0
$\chi_A \times$	$\frac{3s^2}{4}\ln\left(\frac{r_o}{r_i}\right)$	$s^2\left(-\frac{5}{12} - \frac{\cos 2\phi}{8}\left(1 + \frac{r_i^2}{r^2}\right) + \frac{3}{4}\ln\left(\frac{r_o}{r}\right)\right) - \frac{c^2}{6}$	$\frac{s^2\cos 2\phi}{8}\left(\frac{r_o^2 - r_i^2}{r^2}\right)$

Frequency perturbation, $(\Delta\omega(\mathbf{r})/\omega_0)$, in the internal ($r < r_i$), annular ($r_i < r < r_o$), and external ($r > r_o$) compartments of the hollow cylinder model, are listed for the three different contrast mechanisms (isotropic magnetic susceptibility, χ_I, exchange, E, and anisotropic magnetic susceptibility, χ_A). In these expressions $\sin^2\theta$ and $\cos^2\theta$ have been shortened to s^2 and c^2 respectively, and ϕ is the azimuthal angle.

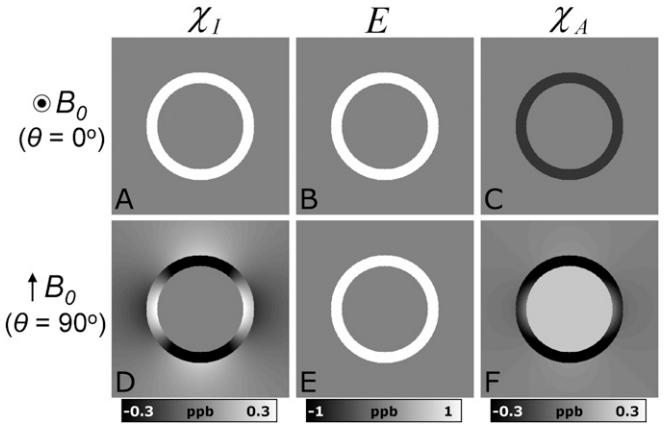

Fig. 4. Calculated field perturbations due to the hollow cylinder model populated with isotropic susceptibility (*A* and *D*), exchange-related field offsets (*B* and *E*), and radially oriented anisotropic susceptibility (*C* and *F*). The field perturbations are simulated with the cylinder axis (fiber orientation) parallel to B_0, $\theta = 0°$ (*A*–*C*), and with the cylinder axis perpendicular to B_0, $\theta = 90°$ (*D*–*F*). The fields are simulated for a g-ratio (r_i/r_o) of 0.8. For ease of comparison, the results are shown for the relevant perturbation (χ_I, *E*, or χ_A) set equal to 1 ppb.

nonlocal fields can be formed. The resulting map is model specific, because it depends on the values of χ_I, E, and χ_A used in estimating the local frequency offset (i.e., the frequency offset in a voxel due to the myelin in that voxel); comparing it to an appropriate simulation of the nonlocal field distribution due to the anatomical distribution of WM and GM provides a further test of the model's validity. For such simulations, forward field calculations (9, 10) were carried out using susceptibility distributions based on segmented GM/WM tissue masks generated from T_1-weighted images of each subject. The nonlocal field offsets due to the difference in both the isotropic and anisotropic susceptibility of WM compared with GM were calculated and fitted to the measurements (*SI Text*). Because we assumed that the susceptibility of GM is isotropic, this approach required the fitting of only one further variable parameter, representing the average isotropic susceptibility offset, χ_{I-LP}, of the large (non-myelin) pool of WM, relative to GM.

Fitting was carried out for the mechanism combinations and associated parameter sets that had yielded good fits to the local frequency variation (Fig. 2). However, the g-ratio was fixed at a value of 0.8 (the best fit value in Table 2) to reduce the computational time. The average difference between the simulated and estimated nonlocal fields was calculated over WM voxels for each subject. If the average difference over the five subjects was significantly different from zero, the underlying model was rejected. Fig. 5 shows results from one subject, calculated using the parameters that gave the smallest differences for the different mechanism combinations. For the $\chi_I + \chi_A$ and $\chi_I + E + \chi_A$ combinations, the simulated nonlocal field offsets in WM (Fig. 5 *E* and *F*) are in reasonable agreement with the model-based estimates from the experimental data (Fig. 5 *B* and *C*). However, for the $\chi_I + E$ combination, the generally negative model-based offsets (Fig. 5*A*) do not match the simulated data (Fig. 5*D*). These results show that only the fiber model combinations including susceptibility anisotropy produce nonlocal fields that are consistent with simulations based on the anatomical distribution of WM and GM (Fig. S1). Table 3 details the parameter values for each mechanism combination that produced the best fit to the local data (Fig. 2), as well as yielding a nonlocal field distribution that was in good agreement with the simulated offsets (Fig. 5).

Discussion

Hollow Cylinder Model. The results presented here show that the fiber orientation-dependent GE contrast (phase and magnitude) measured in vivo in WM can be explained using a simple model in which the myelin sheath is represented as a hollow cylinder composed of material with a small T_2 and anisotropic magnetic susceptibility. The fiber orientation-dependent change in apparent frequency with TE results from the combination of two effects: the loss of the signal from the myelin compartment at long TE and the dependence of the frequency offset in the myelin sheath on its orientation to the applied field. The dependence of the rate of decay of the magnitude signal on fiber orientation is a consequence of the orientation-dependent change in the spatial variation of frequency, and consequent signal dephasing, which is produced by the myelin sheath. The spatially varying fields increase monotonically in strength as fiber orientation varies from parallel to perpendicular, producing a corresponding increase in R_2^*.

Failure of the Model in Which Myelin Has Purely Isotropic Susceptibility. It was necessary to include anisotropic susceptibility or exchange in the model of the myelin compartment to explain the fiber orientation-dependent variation of frequency difference and signal magnitude with TE, because the average relative frequency offset inside the material of a hollow cylinder of purely isotropic susceptibility varies from $\chi_I/3$ to $-\chi_I/6$ as the fiber orientation varies from parallel to perpendicular (Fig. 4 and Table 1), thus producing frequency differences that range over negative and positive values. In contrast, the measured frequency differences are negative at long TE values for all fiber orientations (Fig. 2*B*). Adding the effect of either radial anisotropic susceptibility and/or exchange can produce a frequency difference that is negative for all fiber orientations. However, it was not possible to explain the measured frequency evolution, when considering nonlocal effects (Fig. 5), without incorporating the effect of anisotropic susceptibility (i.e., the $\chi_I + E$ model failed to fit the data). The fit including all three mechanisms ($\chi_I + E + \chi_A$) had a significantly lower residual ($P < 0.05$ via F test on residuals in Table 3) than the fit excluding an exchange component ($\chi_I + \chi_A$), suggesting that an exchange contribution should be included in an accurate myelin model. In the following, we consider the implications of the hollow cylinder model and the parameter values that yield the best overall fit to the experimental data ($\chi_I + E + \chi_A$ in Table 3).

Table 2. Mechanism combinations and associated parameter values that best fitted the measured magnitude and frequency difference data shown in Fig. 2

Mechanism combination	$T_{2\text{-}SP}$, ms	$T_{2\text{-}LP}$, ms	χ_I, ppb	E, ppb	χ_A, ppb	ρ	g-ratio	chi^2
$\chi_I + E$	8 ± 2	36 ± 2	−160 ± 20	50 ± 10	—	0.8 ± 0.1	0.8 ± 0.1	0.37
$\chi_I + \chi_A$	8 ± 2	38 ± 2	−60 ± 20	—	−140 ± 20	0.8 ± 0.1	0.8 ± 0.1	0.38
$\chi_I + E + \chi_A$	8 ± 2	36 ± 2	−100 ± 20	20 ± 10	−100 ± 20	0.7 ± 0.1	0.8 ± 0.1	0.25

The quoted error is the step length of the fitting algorithm. Also shown is the reduced chi-squared residual for each fit. If the residual was higher than 1.14 ($P < 0.05$), the fit was deemed unsuccessful.

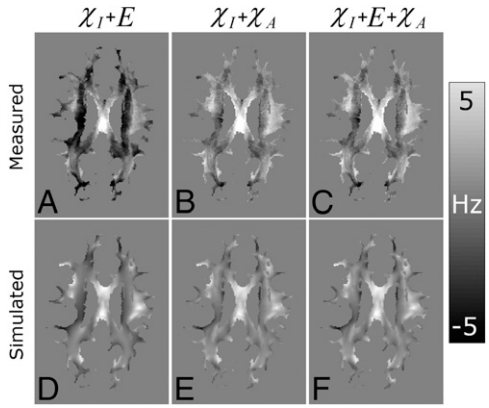

Fig. 5. Comparison of estimates of the nonlocal frequency offsets in WM voxels produced by applying the hollow cylinder model to the measured data (*A*–*C*) and by simulation of the field perturbation produced by the anatomical arrangement of GM and WM (*D*–*F*). Maps were generated for the $\chi_I + E$ (*A* and *D*), $\chi_I + \chi_A$ (*B* and *E*), and $\chi_I + E + \chi_A$ (*C* and *F*) mechanism combinations using the model parameters that yielded the lowest average difference values. By subtracting the simulated nonlocal offsets (*D*–*F*) from the measured offsets (*A*–*C*), difference values were formed for each subject.

Magnetic Susceptibility of Myelin and WM. The anisotropy of the magnetic susceptibility of the myelin can be characterized by the absolute difference in the magnitudes of the principal components of the cylindrically symmetric susceptibility tensor, which takes a value of $3\chi_A/2 = -180 \pm 30$ parts per billion (ppb). This value is consistent in magnitude and sign with the value of ~−200 ppb, which was estimated by Lounila et al. (19) for the oriented lipids in lipoprotein shells. We can also estimate the difference in the average WM volume susceptibility when fibers are oriented perpendicular and parallel to B_0; using the hollow cylinder model, this is given by $-3\nu\chi_A/4 = 16 \pm 3$ ppb (18) (where $\nu = FVF \times [1 - \text{g-ratio}^2]$ is the volume fraction of myelin). This result is close to the value of 12 ppb estimated by Lee et al. (2) in an MRI study of postmortem tissue samples and also of similar magnitude to the 22 ± 8 ppb value, which was recently reported by Li et al. (18) based on in vivo susceptibility mapping experiments. These values were, however, estimated from phase measurements without accounting for the loss of signal from the myelin sheath, and therefore need to be interpreted with some care. From the fitting parameters, the average isotropic susceptibility difference between WM and GM is found to be $\chi_{I-LP} + \nu\chi_I = -30 \pm 10$ ppb, which is in approximate agreement with the previously reported in vivo estimate of ~−50 ppb (23).

Myelin Water Pool. The contribution of the myelin water (small pool) to the total voxel signal (at TE = 0) is given by $\nu\rho = 12.6 \pm 2\%$ (Table 3), which is close to the average myelin water fraction of 11% measured by Laule et al. (13) using a T_2-based approach at 1.5 T. The fitted value of the relative proton density ($\rho = 0.7$) is higher than the expected value of ~0.5 based on the known water content of the different WM compartments (24), most likely as a result of a relative enhancement of the GE signal from the myelin compartment due to the low T_1 of myelin water (22). The fitted T_2 of the myelin water compartment was ~10 ms (Table 3), which is somewhat longer than the T_2^* value of 6 ms recently estimated by van Gelderen et al. (22). This discrepancy is not surprising, because we have estimated T_2 rather than T_2^* by separating off the effects of myelin sheath-induced frequency dispersion. The fitted exchange value of 10 ppb (Table 3) yields an average WM exchange-related frequency offset, relative to GM, of ~1 ppb, which is lower than, but of the same sign as, the 6- to 13-ppb exchange-induced frequency offset range measured by Shmueli et al. (11) on postmortem brain tissue samples.

Implications for Phase Contrast. Dramatic differences are observed in phase-based frequency maps acquired at short TE relative to similar maps acquired at longer TE (Fig. 1). These results represent in vivo evidence for a significant local frequency offset in WM at long TE, which is dependent on microstructure, as predicted by He and Yablonskiy (25). However, the theoretical framework used by these authors, which assumed purely isotropic susceptibility and a cylindrical Lorentz cavity with its axis parallel to the fiber direction, does not explain the orientation-dependent frequency differences that we measured in WM. In this study, we have shown that radial susceptibility anisotropy in the myelin sheath is needed to explain these effects and must therefore be included in an accurate myelin model. In particular, this anisotropy generates an average frequency offset that is positive in the myelin, but negative inside the lumen. Reduction of the signal from the myelin compartment consequently leaves a negative local frequency offset in WM relative to GM, which is strongest in fibers that are perpendicular to the field. This local frequency difference may in part explain the fact that the boundaries between GM and WM in phase images acquired at long TE appear sharper than is predicted from simulations of the frequency offset due to isotropic susceptibility differences (16). The work presented here clearly demonstrates that frequency maps created from GE phase images acquired at long TE do not fully represent the frequency perturbations due to the myelin compartment. The implications of this finding need to be carefully considered in studies using phase data to calculate quantitative information about differences in WM/GM tissue composition (18, 23).

Limitations of the Hollow Cylinder Model. Although the hollow cylinder model successfully describes the orientation-dependent contrast observed in WM, it is clearly a simplistic representation of the myelin sheath. The fitting yields g-ratio values of ~0.8 (Table 2), which are larger than the expected average value of ~0.6 (14), suggesting that the hollow cylinder model underestimates the thickness of the myelin sheath. A possible explanation for this underestimation is the laminar nature of the myelin sheath, which consists of repeating units formed from extracellular and cytoplasmic layers, separated by a lipid bilayer (17). It is likely that the water content and magnetic properties of each sublayer of the myelin sheath unit are very different from one another. An improvement on the model used here would be to break up the homogeneous cylindrical sheath into a series of

Table 3. Mechanism combinations and associated parameter values that best fitted the local frequency variation with TE (Fig. 2), as well as yielding a nonlocal field in good agreement with simulated nonlocal offsets due to the WM/GM anatomy (Fig. 5)

Mechanism combination	$T_{2\text{-}SP}$, ms	$T_{2\text{-}LP}$, ms	χ_I, ppb	E, ppb	χ_A, ppb	ρ	χ_{I-LP}, ppb	chi^2
$\chi_I+\chi_A$	10 ± 2	38 ± 2	−60 ± 20	—	−120 ± 20	0.9 ± 0.1	−20 ± 10	0.70
$\chi_I+E+\chi_A$	10 ± 2	36 ± 2	−60 ± 20	10 ± 10	−120 ± 20	0.7 ± 0.1	−20 ± 10	0.59

The errors and residuals are also displayed, as described in Table 2. The g-ratio was fixed at 0.8 (best-fit value from Table 2) to reduce simulation time.

layers representing different water pools. Another extension to the model would be to include the effects of water diffusion in and between compartments. Diffusion in the inhomogeneous field outside the myelin sheath could lead to a reduction in dephasing, thus affecting the rate of decay of the signal magnitude, but the low diffusion coefficient of myelin water (26) means that the frequency difference values are unlikely to be significantly affected by diffusion.

Applications of Frequency Difference Mapping. Frequency difference mapping forms a powerful method for investigating WM microstructure; unlike phase mapping (1), it is insensitive to nonlocal frequency offsets produced by large anatomical structures and by external sources of field inhomogeneity, and in contrast to susceptibility mapping (23) and susceptibility tensor imaging (9), it does not require the solution of an ill-posed inverse problem. Data acquisition for frequency difference mapping is very simple, relying only on the use of multiecho gradient echo sequences, which are available on all modern scanners, and useful FDM can be generated from images acquired at just two echo times (Fig. 1). Because the frequency difference in WM is dependent on the sheath geometry (g-ratio and FVF) and orientation, FDM may in the future be used in conjunction with fiber orientation information from diffusion tensor images for inferring local information about axonal structure. Conversely, when it is possible to make multiple measurements with WM fibers oriented at different angles to the magnetic field, FDM may potentially be used to identify local fiber orientation. Because such measurements are based on standard GE MRI, it may be possible to generate high-resolution fiber orientation maps in this manner.

Materials and Methods

Data Acquisition. Data were acquired in vivo with the approval of the University of Nottingham's Medical School Research Ethics Committee and all subjects gave informed consent. The GE data were acquired using a Philips Achieva 7T scanner. High-resolution data were acquired from three subjects using a 32-channel receiver coil with a 3D GE sequence [repetition time (TR) 36 ms; flip angle 14°; field of view (FOV) 224 × 224 × 50 mm^3; in-plane resolution 0.6 mm; slice thickness 1.2 mm; scan time 5 min]. For the main data acquisition, subjects were imaged using a 3D GE sequence involving the acquisition of a train of 15 echoes (ΔTE 2 ms; TR 38 ms; flip angle 14°; FOV 224 × 224 × 50 mm^3; isotropic resolution 1 mm; scan time 4 min) with the slab of 50 axial images centered on the corpus callosum. Four image datasets were acquired from each subject, with the time of the first echo, TE_1, varied from 2 to 5 ms in 1-ms steps. To avoid potential confounding effects from small differences between echoes formed under positive and negative read gradients, only the images from the odd echoes of the echo train were used in the analysis. Combination of datasets thus provided 32 images at evenly spaced echo times ranging from 2 to 33 ms. DTI (TE 57 ms; TR 8.6 s; FOV 224 × 224 × 104 mm^3, in-plane resolution 2 mm; slice thickness 2 mm; scan time 7 min; 32 diffusion gradient directions, b-value 1,000 s mm^{-2}) and magnetization-prepared rapid gradient echo (MPRAGE; TE 3.7 ms; TR 8 ms; inversion time 960 ms; long TR 2.8 s; turbo field echo factor 205; flip angle 8°; FOV 256 × 256 × 160 mm^3; isotropic resolution 1 mm) data were acquired on all subjects at 3 T, also using a 32-channel head coil.

Data Processing. Image data were coregistered using FSL FLIRT (27). Phase maps were unwrapped using a 3D algorithm (23), and frequency maps were then created from the high-resolution data by scaling the resulting phase data by 2πTE. For the main study, the phase map measured at TE 2 ms was subtracted from the other phase images before dividing by an effective echo time of (TE-2ms) to yield frequency maps with reduced sensitivity to any transmit-rf phase effects (23). All frequency maps were high-pass filtered using the SHARP method (23). The filtered frequency maps exhibited frequency offsets that varied slowly with spatial position, and these were removed by subtraction of a sixth-order 3D polynomial fit. The magnitude data were normalized relative to the first TE data. The DTI data were processed using the FSL DTIFIT software (28) to yield eigenvectors and fractional anisotropy (FA) maps. The primary eigenvectors were then used to produce the fiber orientation maps. For analysis of the orientation-dependent frequency offsets in WM, FSL FAST (29) was used to segment the MPRAGE data. WM voxels with FA <0.25 were not used in further analysis to ensure reliability of the fiber orientation information. The process for fitting the parameters of the hollow cylinder model involved iteratively varying each parameter over a sensible range, using a step length chosen to give a compromise between accuracy and fitting time. A detailed description of the fitting methods, including parameter ranges, is listed in *SI Text*. The quoted errors for all fitted parameters are equal to the relevant step lengths.

ACKNOWLEDGMENTS. This research was supported by Medical Research Council Programme Grant G0901321 and Engineering and Physical Sciences Research Council Fellowship Grant EP/I026924/1 (to S.W.).

1. Duyn JH, et al. (2007) High-field MRI of brain cortical substructure based on signal phase. *Proc Natl Acad Sci USA* 104(28):11796–11801.
2. Lee J, et al. (2010) Sensitivity of MRI resonance frequency to the orientation of brain tissue microstructure. *Proc Natl Acad Sci USA* 107(11):5130–5135.
3. Denk C, Hernandez Torres E, MacKay A, Rauscher A (2011) The influence of white matter fibre orientation on MR signal phase and decay. *NMR Biomed* 24(3):246–252.
4. Lee J, et al. (2011) T2*-based fiber orientation mapping. *Neuroimage* 57(1):225–234.
5. Bender B, Klose U (2010) The in vivo influence of white matter fiber orientation towards B(0) on T2* in the human brain. *NMR Biomed* 23(9):1071–1076.
6. Sati P, et al. (2012) In vivo quantification of T2 anisotropy in white matter fibers in marmoset monkeys. *Neuroimage* 59(2):979–985.
7. Lee J, et al. (2012) The contribution of myelin to magnetic susceptibility-weighted contrasts in high-field MRI of the brain. *Neuroimage* 59(4):3967–3975.
8. Liu C, Li W, Johnson GA, Wu B (2011) High-field (9.4 T) MRI of brain dysmyelination by quantitative mapping of magnetic susceptibility. *Neuroimage* 56(3):930–938.
9. Liu C (2010) Susceptibility tensor imaging. *Magn Reson Med* 63(6):1471–1477.
10. Marques JP, Bowtell R (2005) Application of a Fourier-based method for rapid calculation of field inhomogeneity due to spatial variation of magnetic susceptibility. *Concepts Magn Reson B Magn Reson Eng* 25B(1):65–78.
11. Shmueli K, Dodd SJ, Li TQ, Duyn JH (2011) The contribution of chemical exchange to MRI frequency shifts in brain tissue. *Magn Reson Med* 65(1):35–43.
12. Zhong K, Leupold J, von Elverfeldt D, Speck O (2008) The molecular basis for gray and white matter contrast in phase imaging. *Neuroimage* 40(4):1561–1566.
13. Laule C, et al. (2004) Water content and myelin water fraction in multiple sclerosis. A T2 relaxation study. *J Neurol* 251(3):284–293.
14. Stikov N, et al. (2011) Bound pool fractions complement diffusion measures to describe white matter micro and macrostructure. *Neuroimage* 54(2):1112–1121.
15. MacKay A, et al. (1994) In vivo visualization of myelin water in brain by magnetic resonance. *Magn Reson Med* 31(6):673–677.
16. Schäfer A, Wharton S, Gowland P, Bowtell R (2009) Using magnetic field simulation to study susceptibility-related phase contrast in gradient echo MRI. *Neuroimage* 48(1):126–137.
17. De Felici M, et al. (2008) Structural characterization of the human cerebral myelin sheath by small angle x-ray scattering. *Phys Med Biol* 53(20):5675–5688.
18. Li W, Wu B, Avram AV, Liu C (2012) Magnetic susceptibility anisotropy of human brain in vivo and its molecular underpinnings. *Neuroimage* 59(3):2088–2097.
19. Lounila J, Ala-Korpela M, Jokisaari J, Savolainen MJ, Kesäniemi YA (1994) Effects of orientational order and particle size on the NMR line positions of lipoproteins. *Phys Rev Lett* 72(25):4049–4052.
20. Rosenblatt C, Yager P, Schoen PE (1987) Orientation of lipid tubules by a magnetic field. *Biophys J* 52(2):295–301.
21. Durrant CJ, Hertzberg MP, Kuchel PW (2003) Magnetic susceptibility: Further insights into macroscopic and microscopic fields and the sphere of Lorentz. *Concepts Magn Reson A* 18A(1):72–95.
22. van Gelderen P, et al. (2012) Nonexponential T2 decay in white matter. *Magn Reson Med* 67(1):110–117.
23. Schweser F, Deistung A, Lehr BW, Reichenbach JR (2011) Quantitative imaging of intrinsic magnetic tissue properties using MRI signal phase: An approach to in vivo brain iron metabolism? *Neuroimage* 54(4):2789–2807.
24. van der Knaap MS, Valk J (2005) *Magnetic Resonance of Myelination and Myelin Disorders* (Springer, New York).
25. He X, Yablonskiy DA (2009) Biophysical mechanisms of phase contrast in gradient echo MRI. *Proc Natl Acad Sci USA* 106(32):13558–13563.
26. Harkins KD, Dula AN, Does MD (2012) Effect of intercompartmental water exchange on the apparent myelin water fraction in multiexponential T2 measurements of rat spinal cord. *Magn Reson Med* 67(3):793–800.
27. Jenkinson M, Smith S (2001) A global optimisation method for robust affine registration of brain images. *Med Image Anal* 5(2):143–156.
28. Behrens TEJ, et al. (2003) Characterization and propagation of uncertainty in diffusion-weighted MR imaging. *Magn Reson Med* 50(5):1077–1088.
29. Zhang Y, Brady M, Smith S (2001) Segmentation of brain MR images through a hidden Markov random field model and the expectation-maximization algorithm. *IEEE Trans Med Imaging* 20(1):45–57.